Sustainable Energy & Fuels
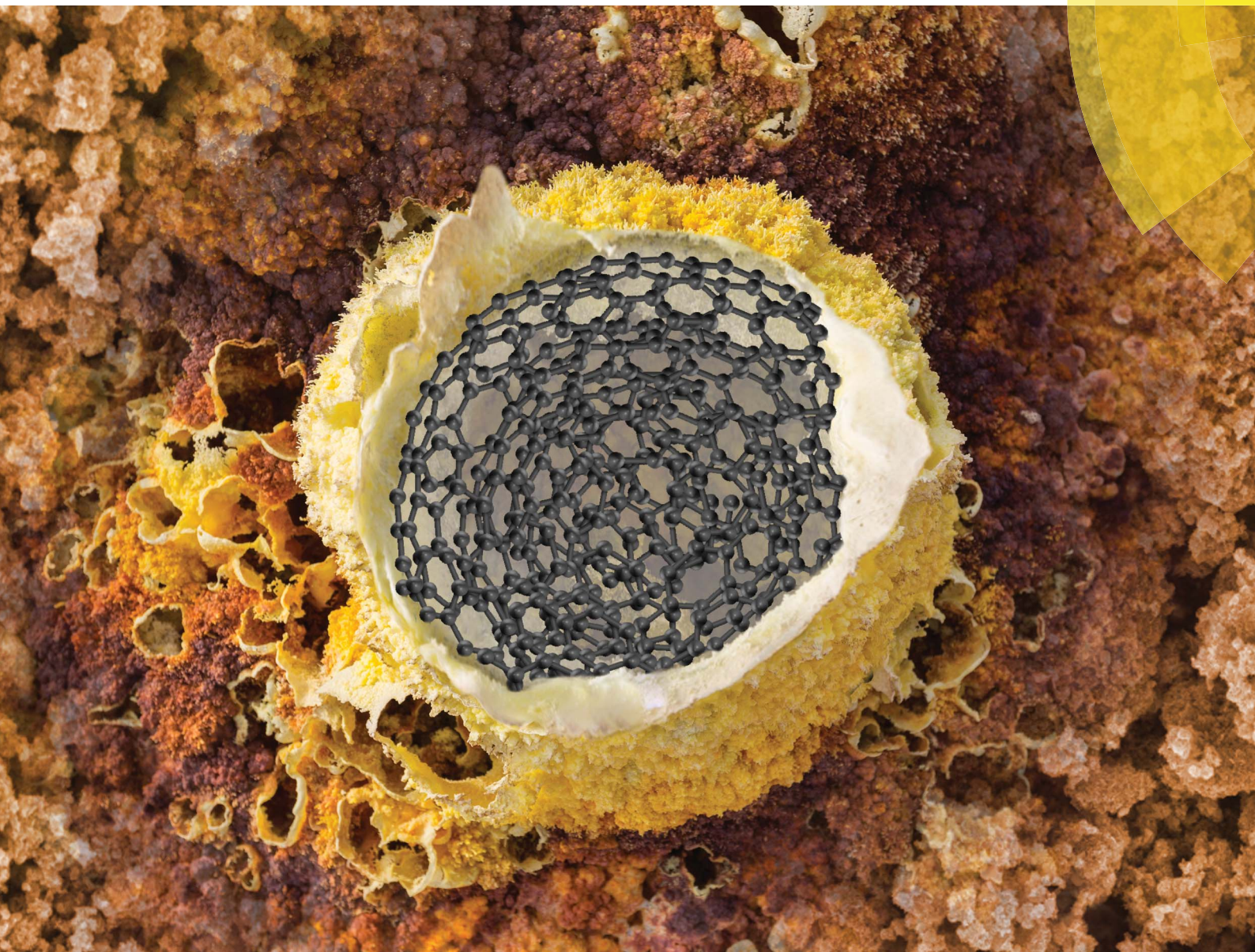
Interdisciplinary research for the development of sustainable energy technologies

rsc.li/sustainable-energy

ROYAL SOCIETY
OF CHEMISTRY

PAPER
Volker Presser *et al.*
Carbon onion–sulfur hybrid cathodes for lithium–sulfur batteries

PAPER

CrossMark
click for updates

Carbon onion–sulfur hybrid cathodes for lithium–sulfur batteries†

Soumyadip Choudhury,[ab] Marco Zeiger,[ac] Pau Massuti-Ballester,[ac] Simon Fleischmann,[c] Petr Formanek,[b] Lars Borchardt[d] and Volker Presser*[ac]

In this study, we explore carbon onions (diameter below 10 nm), for the first time, as a substrate material for lithium sulfur cathodes. We introduce several scalable synthesis routes to fabricate carbon onion–sulfur hybrids by adopting *in situ* and melt diffusion strategies with sulfur fractions up to 68 mass%. The conducting skeleton of agglomerated carbon onions proved to be responsible for keeping active sulfur always in close vicinity to the conducting matrix. Therefore, the hybrids are found to be efficient cathodes for Li–S batteries, yielding 97–98% Coulombic efficiency over 150 cycles with a slow fading of the specific capacity (*ca.* 660 mA h g^{-1} after 150 cycles) in long term cycle test and rate capability experiments.

1. Introduction

The increase in global energy demand and limited reserve of fossil fuel resources have led to intense research efforts for efficient and mobile energy storage technologies, especially rechargeable batteries.[1] The further implementation of current lithium-ion battery technology is impeded by high costs, safety concerns, and the limited energy density associated with state-of-the-art insertion-compound electrodes like layered $LiCoO_2$, spinel $LiMn_2O_4$, olivine $LiFePO_4$ cathodes, and graphite anodes.[2,3] The development of alternative low-cost, abundant electrode materials with high energy and power densities is crucial for widely employing rechargeable batteries for the storage of renewable energies and the transportation sectors.[4,5]

Lithium–sulfur (Li–S) systems have emerged in recent years as a promising battery class.[6–9] In addition to the high specific capacity, using sulfur as a cathode material has the advantages of high natural abundance, low cost, and high environmental friendliness.[7] Although the lithium–sulfur system operates at a relatively low average potential of 2.1 V against Li/Li$^+$, it shows a very high theoretical specific capacity of 1675 mA h g^{-1} and a high theoretical specific energy of 2600 W h kg^{-1}.[5,10] A remaining hindrance to reach the theoretical limit is the low

sulfur utilization for Li–S rechargeable systems. Still, Li–S batteries suffer from the isolative behavior of the start (S_8) and end product (Li_2S), active material loss by dissolution of inter-mediate species (polysulfides) in the electrolyte, and shuttle mechanisms leading to anode passivation by the deposition of Li_2S_2 and Li_2S.[11,12]

Several studies have shown different carbons as a conductive substrate for insulating sulfur including a variety of carbons with a high surface area and conductivity. Among others, researchers have investigated multi-walled carbon nanotubes,[13–15] meso-porous carbon,[16] graphene,[14,17] carbide-derived carbon,[18] biomass derived carbon,[19,20] three-dimensional bicontinuous gyroidal carbon,[21,22] carbon from polyacrylonitrile,[23] activated carbon fiber cloth,[24] and hard[25] or soft templated carbons[26] as substrates for sulfur in lithium–sulfur batteries.

In this work, we explore carbon onions for lithium sulfur batteries. Carbon onions, also known as onion-like carbon (OLC), consist of several concentrically stacked graphitic carbon spheres.[27] A facile and scalable synthesis route for carbon onions is thermal annealing of nanodiamond powder in an inert atmosphere or vacuum.[28] During the annealing process at temperatures above 1300 °C, the sp^3-hybridized nanodiamond is progressively converted to quasi-spherical sp^2-carbon onions.[29] The high electrical conductivity of carbon onion aggregates (*ca.* 4 S cm^{-1}) provides a conductive network for sulfur, while the enhanced surface area (200–600 m^2 g^{-1}) and nanoscopic size (5–10 nm),[30] hierarchical porous structure, and possibility to create a mechanically robust electrode structure are attractive for creating a large sulfur/electrolyte interface, mitigating polysulfide shuttling. Our work compared different synthesis approaches for obtaining carbon onion/sulfur electrodes, provides structural and chemical characterization, and benchmarks the resulting electrochemical performance.

aINM – Leibniz Institute for New Materials, Campus D2 2, 66123 Saarbrücken, Germany. E-mail: volker.presser@leibniz-inm.de

bLeibniz-Institut für Polymerforschung Dresden e.V., Hohe Str. 6, 01069 Dresden, Germany

cDepartment of Materials Science and Engineering, Saarland University, Campus D2 2, 66123 Saarbrücken, Germany

dDepartment of Inorganic Chemistry, Technische Universität Dresden, Bergstraße 66, 01062 Dresden, Germany

2. Experimental description

Materials

Nanodiamond powder was purchased from NaBond Technologies. Battery-grade conductive carbon black (C65) was purchased from Imerys. Sodium thiosulfate pentahydrate ($Na_2S_2O_3 \cdot 5H_2O$), elemental sulfur (S_8), polyvinylidene fluoride (PVDF) powder (molecular mass ca. 534 000 g mol^{-1}), N-methyl-2-pyrrolidone (NMP), bis(trifluoromethane)sulfonimide lithium salt (LiTFSI), 1,2-dimethoxyethane (DME), 1,3-dioxolane (DOL), and lithium nitrate ($LiNO_3$) were purchased from Sigma Aldrich, and used without any further purification. Nickel foil with a thickness of 20 μm was procured from Schlenk Metallfolien. Electrochemical grade high purity (99.9%) lithium was purchased from PI-Kem. A trilayer porous polyolefine separator was obtained from Celgard and we used non-woven polypropylene separators from Freudenberg.

Synthesis of carbon onions

Carbon onions were synthesized by thermal annealing of the detonation nanodiamond with a diameter in the range of 4–6 nm (NaBond Technologies). The nanodiamond powder was annealed in an argon atmosphere in a graphite crucible using a water cooled high temperature furnace with a tungsten heater (Thermal Technology) at 1700 °C for 1 h (heating/cooling rate: 20 °C min^{-1}). For more information, see ref. 28.

Preparation of carbon onion–sulfur composites

Herein, three different approaches were investigated (Fig. 1): (1) mechanical melt mixing of sulfur with carbon onions, (2) in situ formation of sulfur nanoparticles on the carbon surface, and (3) melting of the covering nanoparticles to form homogenous layers around the carbon onions. The melt mixing carbon onion–sulfur composite was prepared as follows: 65 mass% elemental sulfur (S_8) were added to 35 mass% of carbon onions. It was primarily mixed in a mortar, and afterwards ball milled to get nearly uniform distribution of the sulfur. The carbon–sulfur composite powder was thermally annealed at 155 °C for 5 h under an argon atmosphere. Using this treatment sulfur is fluid and attains minimum viscosity (ref. 16) so that uniform coverage of sulfur over all the available surface of carbon onion particles was obtained.

For in situ formation of sulfur nanoparticles on the carbon onion surface, 1.55 g of sodium thiosulfate was first dissolved in 40 mL of water. Afterwards, 100 mg of carbon onions was added with subsequent sonication for 30 min under ice-cold water. In the next step, 2.5 mL of 5 M HCl was added dropwise to the system. By this time, sulfur nanoparticles were formed in the mixture. The mixture was left to react for 2 h and was filtered through a 0.2 μm hydrophilic PVDF filter. It was washed with copious amounts of water until pH 7 was achieved. The carbon onion/sulfur mixture was dried at 80 °C under vacuum for 12 h.

For the third OLC-S hybrid, the carbon onions/sulfur nanoparticle mixture was thermally annealed at 155 °C following the same protocol maintained for the first set of samples.

For comparison, electrodes of the same thickness were made with sulfur nanoparticles along with 10 mass% conductive additive (Super C65) and 8 mass% PVDF binder. The slurry was cast onto nickel foil following the same way as done for carbon onion/sulfur hybrids. This electrode is designated as SNP (sulfur nanoparticle) electrode.

Electrode preparation

The three sets of carbon–sulfur composite powders were individually mixed with 8 mass% of PVDF binder in NMP to attain the desired slurry viscosity. The slurry was cast on a nickel current collector, achieving a 300 μm wet electrode thickness, and afterwards dried in an oven operated under vacuum at 60 °C for 12 h to get rid of any traces of solvent. In the dry state, each electrode has a mass loading of 3–4 mg cm^{-2} (corresponding sulfur loading is 2–3 mg cm^{-2}) which is at the level to attain the required areal capacity desired for applications in electrically driven vehicles.[31]
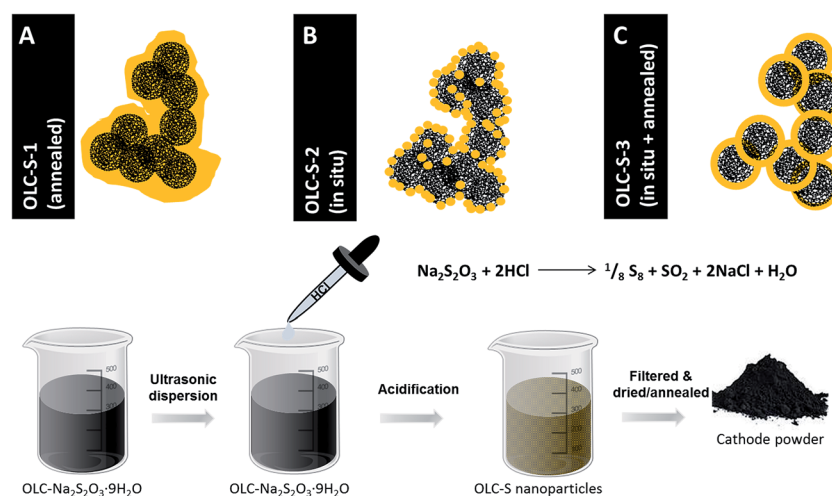

$$Na_2S_2O_3 + 2HCl \longrightarrow \tfrac{1}{8} S_8 + SO_2 + 2NaCl + H_2O$$

Fig. 1 Schematic representation of fabrication of OLC-S hybrids following three different approaches.

Conductivity measurements

The same slurries for each set of samples for preparing electrodes were again cast over 50 μm thin polyimide foil for conductivity measurements. Sheet resistance measurements were made with a custom-built spring-loaded four-point probe with blunt gold contacts (tip diameter: 1.5 mm, tip distance: 3 mm).

Raman spectroscopy

Raman spectra were recorded with a Renishaw inVia Raman Microscope employing an Nd:YAG laser with an excitation wavelength of 532 nm or HeNe laser operating at 633 nm. A grating with 2400 lines per mm and a 50× objective were used to reach a spectral resolution of about 1.2 cm^{-1}. The laser spot on the sample was about 2 μm in diameter at a power of 0.2 mW. The acquisition time of each spectrum was 30 s, and 10 accumulations were averaged.

X-ray diffraction

The crystalline structure of the carbon–sulfur hybrids was analyzed by X-ray diffraction employing a D8 Advance diffractometer (Bruker AXS) with a copper X-ray source (Cu$_{K\alpha}$, 40 kV, 40 mA), a Göbel mirror, and a 2D area detector (VANTEC-500) that covers about 25° 2θ. All samples were measured in a range from 10 to 60° 2θ in 3 steps, with a step duration of 24 min.

Gas sorption measurements

Porosity analysis was carried out using an Autosorb iQ nitrogen gas sorption system (Quantachrome). The carbon onion powder was first outgassed at 300 °C for 10 h under vacuum (10^2 Pa). The nitrogen gas sorption analysis was performed at a temperature of −196 °C in the relative pressure range from 5×10^{-7} to 1.0 in 68 steps. The pore size distribution (PSD) was calculated using the quenched-solid density functional theory (QSDFT)[32,33] supplied by Quantachrome assuming a slit-shape pore geometry. The BET SSA after Brunauer–Emmett–Teller[34] was calculated in the linear regime of the measured isotherms between 0.1 and 0.3P/P_0. Carbon onion sulfur hybrids were not measured using gas sorption analysis due to the evaporation of sulfur and the possible contamination of the system.

Thermogravimetric analysis

To estimate the loading of sulfur in each carbon–sulfur hybrid, thermogravimetric analysis (TGA) was adopted. As sulfur sublimes when heated to 500 °C, TGA of the carbon–sulfur hybrids was performed using a Netzsch Libra TG 209 F1 in the temperature range of 30–500 °C with a heating rate of 10 °C min^{-1} under continuous flow of argon.

CHNS elemental analysis

The chemical composition was further investigated with CHNS elemental analysis with a Vario Micro Cube system (Elementar Analysensysteme). After combustion, the samples were measured under oxygen at 1150 °C in a tin holder. The CHNS analyzer was calibrated with sulfanilic acid using different masses (41.6 mass% C, 4.1 mass% H, 8.1 mass% N, 18.5 mass% S).

Energy filtered transmission electron microscopy

The specimen was prepared by dispersing the powders in ethanol followed by placing a drop on a lacey carbon film TEM grid (Plano GmbH). The TEM grid was dried at 50 °C to remove traces of ethanol before inserting into the TEM instrument. Transmission electron micrographs were recorded with a JEOL 2100F microscope at 200 kV. Energy filtered imaging (EFTEM) was conducted on a Libra 120 transmission electron microscope (Carl Zeiss) operated at 120 keV.

Electrochemical benchmarking

The coin-cell type cathodes were cut as discs of 14.2 mm diameter from the entire piece and 2032 coin cells were assembled in an argon filled glovebox (O_2 & H_2O: <1 ppm) with carbon onion/sulfur hybrid cathodes, lithium metal discs as the anode, and a porous trilayer PP–PE–PP membrane from Celgard and Freudenberg non-woven PP mat together as the separator (PP = polypropylene; PE = polyethylene). Each electrode has a sulfur loading of *ca.* 60 mass% (excluding binder). The separators were soaked with 100 μL of 1 M LiTFSI in 1 : 1 (by volume; v/v) 1,2-dimethoxyethane (DME) and 1,3-dioxolane (DOL) along with 0.25 M LiNO$_3$ serving as the electrolyte. Cyclic voltammetry was performed with a Biologic VPM-300 potentiostat–galvanostat within the potential range of 1 V to 3 V *versus* Li/Li$^+$ at a scan rate of 100 μV s^{-1} (equivalent to 0.2C). Galvanostatic charge/discharge tests were carried out with an Astrol BatSmall battery analyzer at a constant current density of 336 mA g^{-1} (=0.2C) for charging and 168 mA g^{-1} (=0.1C) for discharging within the potential window of 1.8 V to 2.6 V *versus* Li/Li$^+$. The rate capability experiments were done at different rates from 0.1C (discharge)/0.2C (charge) for 20 cycles, 0.2C (discharge)/0.4C (charge) for the next 10 cycles, 0.5C (discharge)/1C (charge) for further 10 cycles, 1C (discharge)/2C (charge) and then brought back to 0.1C (discharge)/0.2C (charge), and allowed to run for the next 20 charging–discharging cycles. For high rate cycle stability tests, the carbon onion hybrid cathode containing cells were subjected to discharge at 1C and charged at 2C for 500 cycles. In all our galvanostatic charge–discharge experiments, we set the charging rate at two times the discharge rate to simulate the actual usage of battery where a faster charging is required.[21]

3. Results and discussion

Carbon onions (OLC) were synthesized by thermal annealing of nanodiamonds (ND) at 1700 °C in argon.[29,30] Using these conditions, ND particles with a mean size of ∼5 nm completely transform to sp^2-hybridized carbon onions. During this process, the diamond structure with a lattice spacing of 0.21 nm rearranges to a graphitic multi-shell carbon onion with an outer lattice spacing of 0.34 nm (Fig. S1, ESI†). Between the single carbon onions with a diameter between 5 and 10 nm, we also

see few-layer graphene nanoribbons as a result of the annealing process (Fig. S1, ESI†).[28]

Carbon onion/sulfur (OLC-S) hybrids were synthesized using three different approaches, as described in the Experimental section. The overall distribution of sulfur on the carbon onion surface and in the interparticle voids was surveyed with energy filtered transmission electron microscopy (EFTEM). The sulfur signal was confirmed by comparing energy filtered images below (153 eV) and above (200 eV) the sulfur ionization edge (165 eV). As seen from Fig. 2B, the *in situ* deposition of sulfur on OLC (OLC-S-2) shows the most uniform sulfur distribution, whereas the melt-mixing (OLC-S-1) leads to a larger degree of localized sulfur clustering (Fig. 2A). Further annealing of *in situ* deposited sulfur on OLC (OLC-S-3) resulted in a low degree of sulfur clustering. Carbon onions act as nucleating surfaces for sulfur nanoparticle deposition, whereas the melt diffusion strategy results in non-uniform spreading of molten sulfur in a random manner. However, the *in situ* sulfur nanoparticle deposition on carbon onion surfaces followed by thermal annealing leads to a low extent of sulfur clustering compared to the mechanical melt mixing pathway, as evident from the carbon–sulfur colored overlay images (Fig. 2C).

The nitrogen gas sorption measurement of carbon onions shows a surface area of 425 m^2 g^{-1} (BET) and 402 m^2 g^{-1} (DFT) with a pore volume of 1.21 cm^3 g^{-1}. The pore size distribution pattern can be differentiated into three regimes: pores related to particles in direct contact (for pores <1 nm), particles separated by spacer particles (at 1 nm pore size and in the mesopore range), and pores between particle agglomerates (Fig. 3A). These spaces among the particle interstices were utilized to embed insulating sulfur to attain a high degree of intimate contact with the carbon onion surfaces. Additionally, the pore hierarchy also plays a crucial role in functioning of lithium–

sulfur batteries by accommodating a large quantity of sulfur mass as well as electrolyte wetting together with lowering the tendency of polysulfide migration out of the cathode to the bulk electrolyte.[15,35–39]

Thermogravimetric analysis of pristine carbon onions undergoes a very little mass loss of *ca.* 1% up to 500 °C. This mass loss is attributed to the decomposition of functional groups on the surface of carbon onions. The thermogravimetric measurements of OLC-S hybrids demonstrate one step mass loss at around 300 °C for all samples with a mass loss of 68% OLC-S-1 and 65% for OLC-S-2 and OLC-S-3 (Fig. 3B). The respective mass loss corresponds to the sulfur content from CHNS elemental analysis (Table 1). The absence of any other step in the thermogram indicates that sulfur is only coated onto the carbon onions and does not penetrate the inside of the particles, irrespective of the deposition process. For contrast, hierarchical porous carbons exhibit more than one step of mass loss during thermogravimetry.[40,41] It is reported in the literature that the sulfur confined in micropores requires a higher thermal energy and is released at much higher temperature than the sulfur present outside the micropores.[40,41]

The structure of carbon onions was not changed by the synthesis procedures as indicated by Raman spectroscopy (Fig. 3C, Table 2, and Fig. S2, ESI†) and XRD (Fig. 3D). Independent of the treatment, carbon onions are characterized by their typical Raman spectrum with the carbon D-mode at 1338 cm^{-1}, the G-mode at 1577 cm^{-1}, and a distinct second order spectrum (Fig. S2, ESI†). The G-mode, representative for sp^2-hybridized carbon, is measured at 1577 cm^{-1}, indicating nanocrystalline and partially amorphous carbon. Amorphous carbon is mostly located between the particles (Fig. S1B, ESI†), leading to partially connected particles and a strong degree of agglomeration. Carbon onions present a rather high degree of
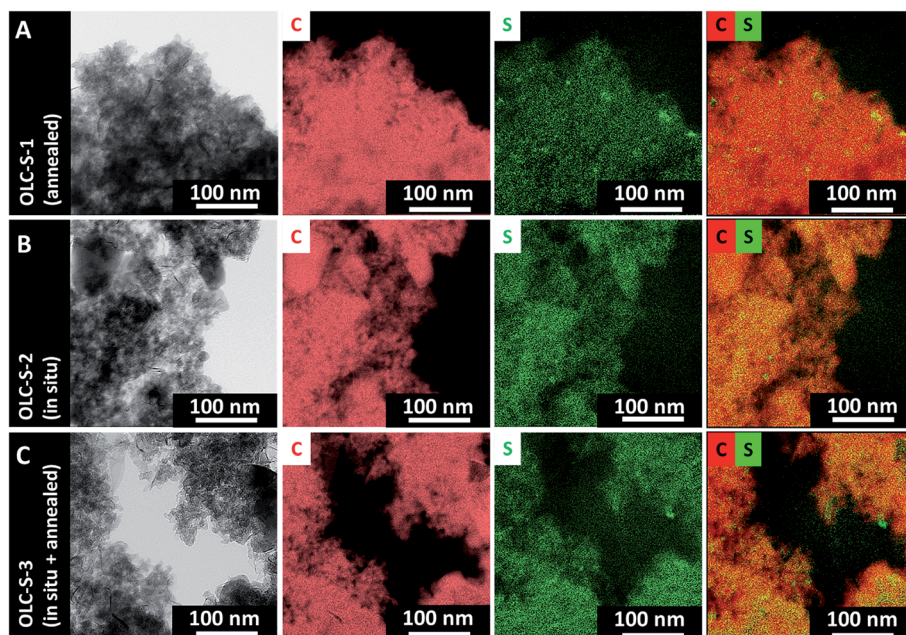

Fig. 2 (A–C) Energy filtered transmission electron micrographs of carbon onion/sulfur hybrid materials, their corresponding elemental maps, and the overlay of carbon and sulfur elemental mappings.
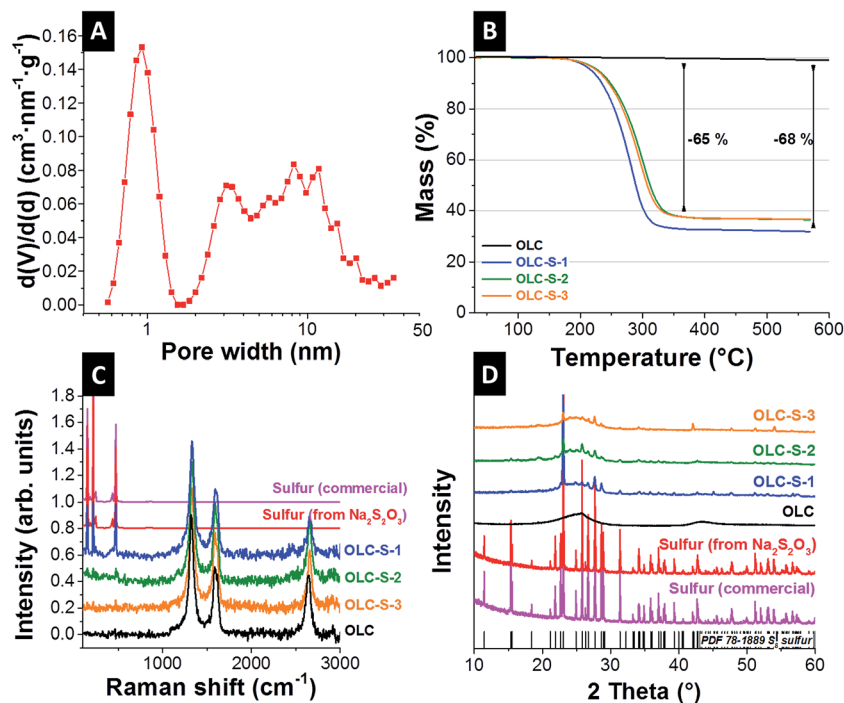
Fig. 3 (A) Pore size distribution of OLC calculated from QSDFT assuming slit pores, (B) sulfur contents from TGA, (C) Raman spectra (633 nm excitation wavelength) and (D) X-ray diffractograms of carbon onions and carbon onion/sulfur hybrids.

Table 1 Estimation of sulfur contents from TGA and CHNS elemental analysis

	Sulfur (mass%)	
Sample	TGA	CHNS
OLC-S-1	68	68 ± 1
OLC-S-2	65	62 ± 5
OLC-S-3	65	64 ± 1

ordering as demonstrated by the sharp G-mode (FWHM of 44 cm^{-1}) and the distinct second order peaks at 2675 cm^{-1}. By virtue of the instability under laser irradiation, we did not detect any sulfur when using a laser wavelength of 532 nm. To avoid such degradation, we conducted also experiments at 633 nm excitation wavelength (Fig. 3C). Commercial sulfur and sulfur derived from sodium thiosulfate were also characterized by Raman spectroscopy. Sulfur shows three distinct peaks at 156, 219, and 473 cm^{-1}, which are related to the vibrations of the S–S bonds.[14,19,42] When measuring the OLC-S hybrids by Raman

spectroscopy, OLC-S-2 and OLC-S-3 showed very weak sulfur signals, whereas OLC-S-1 demonstrated very clearly all three characteristic sulfur peaks. This indicates the presence of non-uniform distributions of sulfur onto the carbon onion surfaces whereas the two other hybrids claim to have nearly homogeneous coverage of sulfur on OLC. As a result, the Raman signals from carbon predominate over sulfur signals although all three hybrids contain *ca.* 65 mass% of sulfur (relative to the carbon mass).

The incompletely crystalline structure of carbon onions was further assessed by XRD (Fig. 3D). The broadening of the (002) graphitic carbon peak at ~26° 2θ is a consequence of the nanoscopic carbon particle size of 5–7 nm. In all three OLC-S hybrids, all crystalline peaks of sulfur are detected in alignment with PDF 78-1889. This confirms the growth of crystalline sulfur domains on the carbon onion substrates and ensures the allocation of sulfur in interparticle voids. When carbon with a large inner porosity is used as the host for sulfur, molten sulfur or nanoparticle precursor solutions tend to infiltrate into the pores driven by capillary forces.[16,24] In such a case, the imbibed sulfur in the pores does not display the well-resolved crystalline

Table 2 Raman spectroscopy results of OLC and OLC-S hybrids

Sample	Position D-band (cm^{-1})	Position G-band (cm^{-1})	FWHM D-band (cm^{-1})	FWHM G-band (cm^{-1})	I_D/I_G
OLC	1338	1580	57	44	1.43
OLC-S-1	1339	1579	67	48	1.79
OLC-S-2	1339	1577	62	46	1.70
OLC-S-3	1338	1576	62	48	1.69

peaks.[16,24] In the OLC-S hybrids, sulfur remains at the exterior surfaces of OLC particles. For this reason, no significant differences were visible in the XRD pattern of three different hybrid types.

The usefulness of the carbon onions as a host for embedding sulfur was further tested by sheet resistance measurements of the 80–100 μm (dry) thick electrodes coated on polyimide foil (Table 3). Using a four-point-probe, the measured electrical conductivity of all samples showed little difference, with values around 0.2 S cm^{-1}.

Electrochemical characterization including cyclic voltammetry (three-electrode setup) and galvanostatic charge–discharge measurements (two-electrode setup) was performed by using the OLC-S composite electrode as the working electrode (cathode) and lithium as the counter electrode (anode)

Table 3 Conductivity measurements *via* the four-point-probe of OLC-S hybrids

Sample	Conductivity (S cm^{-1})
OLC-S-1 electrode	19.8×10^{-2}
OLC-S-2 electrode	23.3×10^{-2}
OLC-S-3 electrode	20.8×10^{-2}

and reference electrode. The cyclic voltammograms show the characteristic shape of sulfur oxidation and reduction (Fig. 4A, C and E). During discharge, the characteristic two reduction peaks at around 2.4 V and 2.0 V *vs.* Li appear (Fig. 4A, C and E). These peaks correspond to the ring opening reduction of sulfur to Li_2S_n ($n > 4$) and the subsequent reduction of higher order polysulfides to short chain polysulfide species, respectively.[43] The anodic sweep shows a characteristic single peak at around 2.4 V *vs.* Li. The relatively narrow peaks for OLC-S-2 and stable peak positions for oxidation and reduction indicate good reaction kinetics for reduction and oxidation reactions in the first cycle and run in a comparable range for all cycles. The two other hybrids OLC-S-1 and OLC-S-3 have much broader oxidation and reduction peaks which are indicative of relatively slow and inferior reaction kinetics compared to OLC-S-2. Such broadening of redox peaks arises from uneven distribution of sulfur in the OLC matrix. Thus, the reaction steps are overlapping and yield broader redox peaks, which indicate poor performances such as low energy efficiency and slow kinetics. The poorer performance can be related to larger amounts of inactive sulfur insufficiently connected to the conductive carbon onion substrate. In the case of OLC-S-3, due to the thermal treatment after nanoparticle formation, the molten sulfur moves to some extent from the surface and reorganizes as larger sulfur
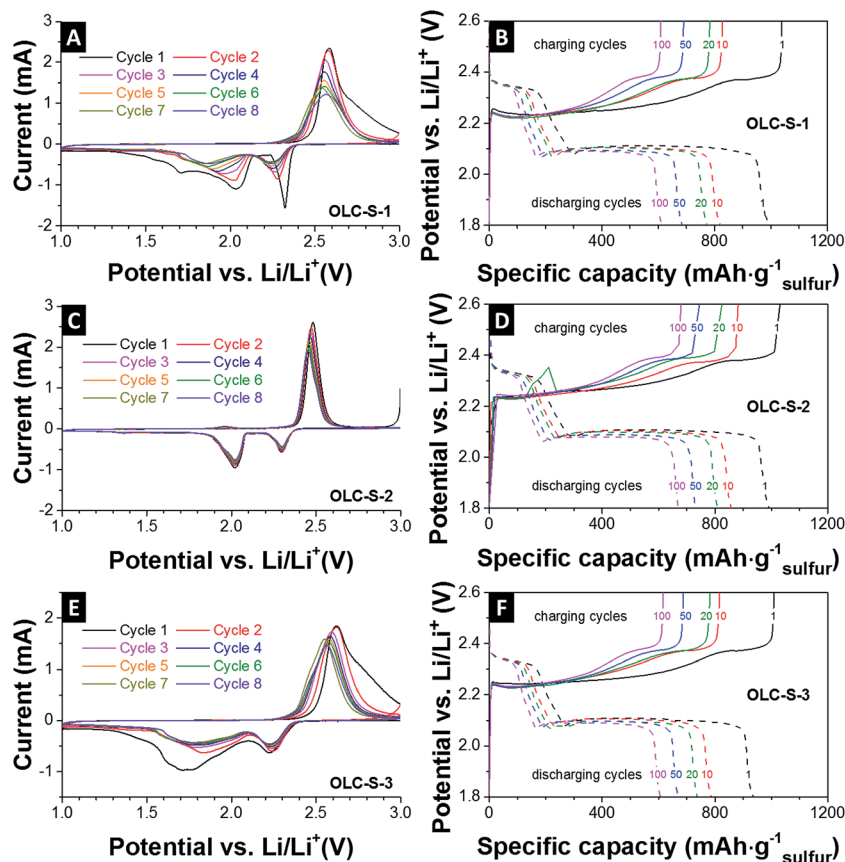

Fig. 4 Cyclic voltammograms at a rate of 0.1 mV s^{-1} and galvanostatic charge–discharge curves at 336 mA g^{-1} (0.2C) for charging and 168 mA g^{-1} (0.1C) for discharging within the potential window of 1.8 V to 2.6 V *versus* Li/Li$^+$ of (A and B) OLC-S-1, (C and D) OLC-S-2, and (E and F) OLC-S-3.

particles, which are not ideally covering the carbon onion surfaces anymore. Those agglomerated parts remain electrochemically inactive, thus demonstrating poorer performance compared to OLC-S-2.

The reversible galvanostatic charge–discharge tests of the OLC-S hybrids were carried out in 2032 coin cells at 0.1C discharge rate (167 mA g^{-1}) and 0.2C charging rate (334 mA g^{-1}). The plateaus in the voltage profiles (Fig. 4B, D and F) match the peak voltages of the cyclic voltammograms for reduction and oxidation (Fig. 4A, C and E). We identify two plateaus in the discharge process, as summarized by Ji *et al.* (ref. 16):

• The first one contributes a minor part to the overall capacity from 2.4 V to *ca.* 2.1 V *vs.* Li. This plateau corresponds to the ring opening conversion of elemental sulfur (S_8) to Li polysulfide anions (Li_2S_x; where x is typically 4–5).[6,7,11] The kinetics of this step are fast.

• The second plateau appears at around 2.1 V *vs.* Li due to the conversion reaction of higher order polysulfides to Li_2S_2 and then to Li_2S. This reaction occurs at a much slower rate and contributes to the large fraction of the overall capacity.

The similarity of voltage profiles at different cycles is indicative of slower capacity fading with prolonged cycling.

Additionally, the voltage plateaus of all samples that appear at the same potential during discharge and charge reflect the mitigation of active mass loss per charging–discharging cycles.

The corresponding specific capacities for charging and discharging are represented normalized to the sulfur mass (Fig. 5A). The specific capacities of all hybrids present values of 900–1200 mA h g$_{sulfur}^{-1}$ in the initial cycles (up to 5 cycles). After 10 charge–discharge cycles, OLC-S-2 and OLC-S-3 hybrids showed only a slow capacity fading per cycles. The capacity stabilized at 800 mA h g$_{sulfur}^{-1}$ and 600 mA h g$_{sulfur}^{-1}$ up to 150 charging–discharging cycles for OLC-S-2 and OLC-S-3 hybrids, respectively. Cathodes containing carbon onions/sulfur hybrids, where the melt diffusion route was followed, demonstrated severe capacity fading within 50 cycles and remained with only 400 mA h g$_{sulfur}^{-1}$ at the end of 150 cycles of charge–discharge. The electrode prepared from sulfur nanoparticles (SNPs) with 10 mass% conductive additive showed a low specific capacity in the initial cycles. After 20 cycles, the specific capacity was stabilized at 200 mA h g$_{sulfur}^{-1}$ for the following 150 cycles. The relatively low specific capacity values are because of an insufficient amount of conducting carbon with a high surface area around the sulfur nanoparticles.
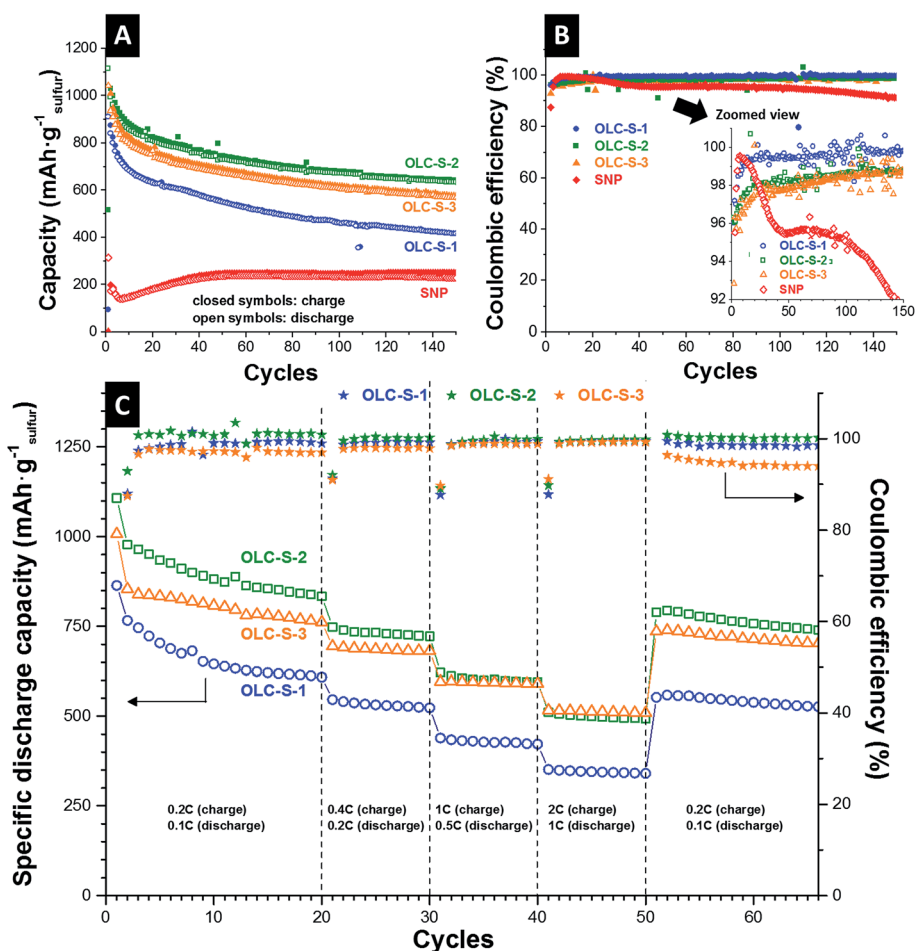

Fig. 5 Cycling performance (0.2C charge, 0.1C discharge) for the (A) specific capacity and (B) Coulombic efficiency (inset shows the zoomed range of 92–100%). (C) Rate capability study of the carbon onion/sulfur hybrid and sulfur nanoparticle (SNP) cathodes.

Table 4 Reported values for selected carbon/sulfur electrodes in comparison to this work. In all reports, metallic Li was used as the anode. Used abbreviations: PC = propylene carbonate; EC = ethyl carbonate; DEC = diethyl carbonate; DME = dimethoxyethane; DOL = 1,3-dioxolane; LiTFSI = Li salt of bis(trifluoromethanesulfonyl)imide; PEGDME = polyethylene glycol dimethyl ether; PYR$_{14}$ = 1-butyl-1-methylpyrrolidinium; TEGDME = tetraethylene glycol dimethyl ether; (w = mass; v = volume)

Carbon for cathode	Surface area (m² g⁻¹)	Sulfur loading (mg cm⁻²)	Separator	Electrolyte	Specific capacity (mA h g$_{sulfur}$⁻¹)			Potential window	C-Rate	Ref.
					Cycle 5	Cycle 50	Cycle 100			
This work	ca. 400	2–3	Polyolefin separators	1 M LiTFSI in 1:1 (v/v) DME/DOL + 0.25 M LiNO₃	ca. 950 (OLC-2)	ca. 730 (OLC-2)	ca. 670 (OLC-2)	1.8–2.6 V	0.1C (discharge), 0.2C (charge)	—
Acetylene black	ca. 65	1.5	Polypropylene separator	1 M LiPF₆ PC/EC/DEC 1:4:5 (v/v)	ca. 600	ca. 500	—	1.8–2.8 V	0.02C	45
Ketjen black	ca. 800	0.81	Unknown	0.5 M LiSO₃CF₃ in 8:2 (v/v) DME/DOL + imidazolium salts	ca. 770	ca. 700	ca. 600	1.8–2.8 V	0.5C	46
Multi-walled carbon nanotube	ca. 107	Unknown	Celgard	0.5 M LiTFSI in 1:1 (v/v) DME/DOL + 0.5 M LiNO₃	ca. 1100	ca. 1000	ca. 950	1.7–2.7 V	0.18C	35
Vertically aligned CNTs	—	Unknown	Celgard and glass fiber mat	1 M LiTFSI in 1:1 (v/v) DME/DOL + 0.25 M LiNO₃	ca. 850	ca. 750 (cycle 40)	—	1–3 V	0.08C	47
Small CNTs confined inside a large CNT	ca. 150	1.36	Unknown	1 M LiTFSI in 1:1 (v/v) DME/DOL	ca. 1250	ca. 1100	ca. 1000	1.5–3 V	0.1C	43
Carbon aerogel	ca. 1395	Unknown	Polypropylene separator	1 M LiTFSI in 1:1 (v/v) DME/DOL + 0.1 M LiNO₃	ca. 790	ca. 650	ca. 600	1.8–2.8 V	0.1C	40
Ordered mesoporous carbon	2445	0.45	Not mentioned	1 M LiTFSI in 1:1 (v/v) DME/DOL	ca. 1000	ca. 900	ca. 800	1.5–3 V	1C	48
Ordered mesoporous carbon (KOH activated)	ca. 1566	0.25	Celgard	1 M LiTFSI in 55:40 (v/v) DME/DOL	ca. 500 (51.5% S)	ca. 300	—	1–3.6 V	1.5C	37
Sulphur–TiO₂ yolk-shell	—	0.4–0.6	Unknown	1 M LiTFSI in 1:1 (v/v) DME/DOL + 0.14 M LiNO₃	ca. 1000	ca. 800	ca. 900	1.7–2.6 V	0.5C	49
Hydrothermal carbon from monosaccharides	ca. 300		Unknown	1 M LiTFSI in 1:1 (v/v) DME/DOL	ca. 780	ca. 580	—	1.5–3.2 V	1C	50
Reduced graphene oxide	—	Unknown	Celgard	LiTFSI in PYR₁₄TFSI/PEGDME (1:1 w/w)	ca. 900	ca. 900	—	1–3 V	0.02C (3 cycles) then 0.1C for 47 cycles	51
Graphene-enveloped sulfur	—	Unknown	Unknown	1 M LiTFSI in TEGDME	ca. 690	ca. 520	—	1.5–3 V	0.2C	17
Nafion coated sandwich type graphene sheets	ca. 578	Unknown	Celgard	1 M LiTFSI in 1:1 (v/v) DME/DOL	ca. 950	ca. 800	—	1–3 V	0.1C	52
Activated carbon fiber cloth	2000	6.5	Celgard	0.35 M LiTFSI in 1:1 (v/v) DME/DOL + 0.29 M LiNO₃	ca. 1000	ca. 950	—	1.7–2.5 V	0.09C	24
Inverse opal carbon	ca. 1300	2–3	Polyolefin separator	1 M LiTFSI in 1:1 (v/v) DME/DOL + 0.25 M LiNO₃	ca. 1650	ca. 400	—	1.5–2.8 V	0.1C	26
3D gyroidal carbon	ca. 900	2–3	Polyolefin separator	1 M LiTFSI in 1:1 (v/v) DME/DOL	ca. 650	ca. 600	ca. 520	1.5–2.8 V	0.1C (discharge), 0.2C (charge)	21
3D gyroidal carbon (activated)	ca. 2000	0.8	Celgard	1 M LiTFSI in TEGDME + 0.15 M LiNO₃	ca. 1100	ca. 1000	ca. 830	1.5–2.8 V	0.1C	22

Additionally, a comparison of specific capacities from the literature with different types of carbon substrates can be found in Table 4.

The capacity loss in the initial cycles can be attributed to the irreversible diffusion of polysulfides possibly from the dissociative sulfur on the surface of OLC particles. This irreversible reaction leads to slightly lower Coulombic efficiency close to 97–99% in reversible (Fig. 5B) or irreversible mode (Fig. 5C). For comparison, the SNP electrodes demonstrated a Coulombic efficiency below 95% after 30 cycles and after 100 cycles, the Coulombic efficiency dropped below 90%. This behavior can be explained by a lack of structural integrity and loss of electrical connectivity between the additive and sulfur nanoparticles. The relatively high specific capacity in the beginning and the slow capacity fading of OLC-S hybrids can be attributed to the benefits of the enhanced surface area of carbon onions and the accessible interparticle space. The interconnecting feature of carbon onion agglomerates provides a high electrical conductivity and is beneficial to ensure accessibility of the active material by the electrolyte and the Li^+ ions with prolonged cycling.

The rate capability tests of the carbon onion–sulfur hybrids were carried out in 2032 coin cells at multiple C-rates (Fig. 5C). The respective charge and discharge protocol is explained in the experimental part. After 20 cycles at a low rate (0.2C charge and 0.1C discharge) and 30 cycles at a high rate (up to 2C charge and 1C discharge) the specific capacity was recovered close to the level of the initial 20th cycles after multiple irreversible charging–discharging fluctuations. From the irreversible capacity retention ability, it can be concluded that the carbon onion–sulfur composite nanostructures were not ruptured and the sulfur distribution was restored even after such stringent charging–discharging conditions.

Finally, we investigated the long-term cycle performance of the OLC-S hybrids at very high C-rates, for instance, 2C (equivalent to 3350 mA g^{-1} with respect to sulfur) for charging and 1C (equivalent to 1675 mA g^{-1} with respect to sulfur) for discharging (Fig. 6). Among all three OLC-S hybrids, the onion-like carbon hybrid fabricated by the *in situ* routine followed by thermal annealing demonstrated an initial specific discharge capacity of 800 mA h g^{-1}. After 25 cycles, the battery showed a very high stability over 500 cycles with a slow rate of capacity fading (Fig. 6). For the latter, we measured a remaining capacity of 400 mA h g^{-1} after 500 cycles. The other *in situ* hybrid

(*i.e.*, without annealing) followed a similar trend, yielding 300 mA h g^{-1} after 500 cycles. The OLC-S hybrid fabricated *via* the melt diffusion strategy had been showing poorest performances amongst all three hybrids due to random distribution of sulfur in the hybrid. The better performance of the OLC-S-3 at higher rates relative to other hybrids was also observed in rate capability experiments (Fig. 5C). The slower capacity fading at such high specific currents is mainly ascribed to the excellent electrical conductivity of the OLC-S hybrids, which are capable of satisfying the requirement for such fast discharge and charge during repetitive cycling.[41,43] We attribute the better performance at higher charge/discharge rates of OLC-S-3 to the much more integrated hybrid nanostructure by melting of the *in situ* deposited sulfur on the surface of OLC. Our findings are also in good agreement with the published reports by Nazar *et al.* performed at high C rates (cut-off voltage limit 1.5–3 V *vs.* Li/Li$^+$) exploiting bimodal porous carbon possessing over 2000 m^2 g^{-1} surface area.[44]

4. Conclusions

Our work introduces carbon onions for the fabrication of carbon/sulfur hybrid cathodes for lithium–sulfur batteries with sulfur loading up to 68 mass% and without any further addition of a conducting aid such as carbon black. Three different approaches were explored: (1) melt diffusion, (2) *in situ* generation of sulfur nanoparticles on the surface of onion-like carbon, and (3) *in situ* generation of sulfur nanoparticles on the surface of onion-like carbon followed by thermal annealing.

The electrochemical performance of these hybrid materials has been tested by electrochemical characterization. Carbon onion–sulfur hybrids prepared *via* the *in situ* approach (OLC-S-2 and OLC-S-3) had an optimum interaction between the hybrid components exhibiting a specific capacity of *ca.* 700 mA h g^{-1} even after 150 charge–discharge cycles at 167 mA g^{-1} specific current (corresponds to 0.1C discharge rate). In addition, the capacity restoration ability of OLC-S *in situ* hybrids right after running with a high current density of 1675 mA g^{-1} (corresponds to 1C discharge rate) demonstrated a specific capacity of 740 mA h g^{-1} close to its earlier capacity at 0.1C rate (800 mA h g^{-1}) when the current density was reduced to 167 mA g^{-1} (corresponds to 0.1C discharge rate). This hybrid material showed enhanced performance compared to the other OLC-S hybrids studied at slow discharge rates. In addition, these hybrids demonstrate good cycle performances operated with very high C-rates (1C for discharge and 2C for charge). Amongst them, the hybrid fabricated *via in situ* generation of sulfur nanoparticles on the surface of onion-like carbon followed by thermal annealing (OLC-S-3) has been found to be superior (800 mA h g^{-1} at cycle 1, 600 mA h g^{-1} at cycle 20, and 400 mA h g^{-1} at cycle 500).

The high electrochemical stability and attractive rate handling can be attributed to carbon onion aggregates which contribute a high electronic conductivity and provide an exclusively outer surface, which enables the synergy of high sulfur mass loading and high percentage of electrochemically active sulfur.
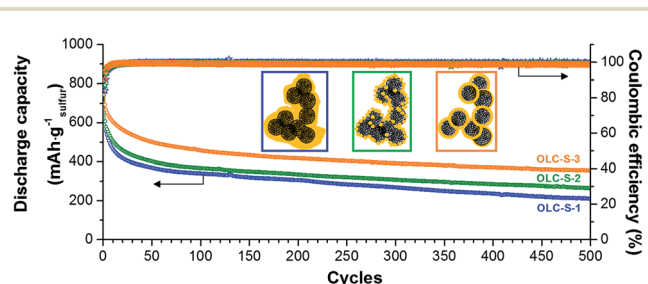

Fig. 6 Long term cycle stability at high C-rates (charging at 2C/discharging at 1C) study of the carbon onion/sulfur hybrids.

Acknowledgements

References

1 B. Dunn, H. Kamath and J.-M. Tarascon, *Science*, 2011, **334**, 928–935.
2 P. G. Bruce, B. Scrosati and J. M. Tarascon, *Angew. Chem., Int. Ed.*, 2008, **47**, 2930–2946.
3 C. M. Hayner, X. Zhao and H. H. Kung, *Annu. Rev. Chem. Biomol. Eng.*, 2012, **3**, 445–471.
4 J. M. Tarascon and M. Armand, *Nature*, 2001, **414**, 359–367.
5 M. M. Thackeray, C. Wolverton and E. D. Isaacs, *Energy Environ. Sci.*, 2012, **5**, 7854–7863.
6 A. Manthiram, S. H. Chung and C. Zu, *Adv. Mater.*, 2015, **27**, 1980–2006.
7 L. Borchardt, M. Oschatz and S. Kaskel, *Chem.–Eur. J.*, 2016, **22**, 7324–7351.
8 G.-L. Xu, Y.-F. Xu, J.-C. Fang, X.-X. Peng, F. Fu, L. Huang, J.-T. Li and S.-G. Sun, *ACS Appl. Mater. Interfaces*, 2013, **5**, 10782–10793.
9 J. Tang, J. Yang and X. Zhou, *RSC Adv.*, 2013, **3**, 16936–16939.
10 M. Wild, L. O'Neill, T. Zhang, R. Purkayastha, G. Minton, M. Marinescu and G. J. Offer, *Energy Environ. Sci.*, 2015, **8**, 3477–3494.
11 M. K. Song, E. J. Cairns and Y. Zhang, *Nanoscale*, 2013, **5**, 2186–2204.
12 X. Ji and L. F. Nazar, *J. Mater. Chem.*, 2010, **20**, 9821–9826.
13 Y.-S. Su, Y. Fu and A. Manthiram, *Phys. Chem. Chem. Phys.*, 2012, **14**, 14495–14499.
14 J. Guo, Y. Xu and C. Wang, *Nano Lett.*, 2011, **11**, 4288–4294.
15 K. Mi, Y. Jiang, J. K. Feng, Y. T. Qian and S. L. Xiong, *Adv. Funct. Mater.*, 2016, **26**, 1571–1579.
16 X. Ji, K. T. Lee and L. F. Nazar, *Nat. Mater.*, 2009, **8**, 500–506.
17 S. Evers and L. F. Nazar, *Chem. Commun.*, 2012, **48**, 1233–1235.
18 T. J. Lee, Y. Zhao, S. Thieme, H. Kim, M. Oschatz, L. Borchardt, A. Magasinski, W. I. Cho, S. Kaskel and G. Yushin, *Adv. Mater.*, 2013, **25**, 4573–4579.
19 F. Chen, J. Yang, T. Bai, B. Long and X. Zhou, *Electrochim. Acta*, 2016, **192**, 99–109.
20 M. Raja, N. Angulakshmi and A. M. Stephan, *RSC Adv.*, 2016, **6**, 13772–13779.
21 S. Choudhury, M. Agrawal, P. Formanek, D. Jehnichen, D. Fischer, B. Krause, V. Albrecht, M. Stamm and L. Ionov, *ACS Nano*, 2015, **9**, 6147–6157.
22 J. G. Werner, S. S. Johnson, V. Vijay and U. Wiesner, *Chem. Mater.*, 2015, **27**, 3349–3357.

23 C. Lai, X. Gao, B. Zhang, T. Yan and Z. Zhou, *J. Phys. Chem. C*, 2009, **113**, 4712–4716.
24 R. Elazari, G. Salitra, A. Garsuch, A. Panchenko and D. Aurbach, *Adv. Mater.*, 2011, **23**, 5641–5644.
25 N. Jayaprakash, J. Shen, S. S. Moganty, A. Corona and L. A. Archer, *Angew. Chem., Int. Ed.*, 2011, **123**, 6026–6030.
26 M. Agrawal, S. Choudhury, K. Gruber, F. Simon, D. Fischer, V. Albrecht, M. Göbel, S. Koller, M. Stamm and L. Ionov, *J. Power Sources*, 2014, **261**, 363–370.
27 M. Zeiger, N. Jäckel, V. N. Mochalin and V. Presser, *J. Mater. Chem. A*, 2016, **4**, 3172–3196.
28 M. Zeiger, N. Jäckel, D. Weingarth and V. Presser, *Carbon*, 2015, **94**, 507–517.
29 V. L. Kuznetsov, A. L. Chuvilin, Y. V. Butenko, I. Y. Mal'kov and V. M. Titov, *Chem. Phys. Lett.*, 1994, **222**, 343–348.
30 M. Zeiger, N. Jäckel, M. Aslan, D. Weingarth and V. Presser, *Carbon*, 2015, **84**, 584–598.
31 D. Lv, J. Zheng, Q. Li, X. Xie, S. Ferrara, Z. Nie, L. B. Mehdi, N. D. Browning, J.-G. Zhang, G. L. Graff, J. Liu and J. Xiao, *Adv. Energy Mater.*, 2015, **5**, 1402290.
32 X. Chen, E. Pomerantseva, P. Banerjee, K. Gregorczyk, R. Ghodssi and G. Rubloff, *Chem. Mater.*, 2012, **24**, 1255–1261.
33 P. I. Ravikovitch, A. Vishnyakov and A. V. Neimark, *Phys. Rev. E: Stat., Nonlinear, Soft Matter Phys.*, 2001, **64**, 011602.
34 S. Brunauer, P. H. Emmett and E. Teller, *J. Am. Chem. Soc.*, 1938, **60**, 309–319.
35 J.-J. Chen, Q. Zhang, Y.-N. Shi, L.-L. Qin, Y. Cao, M.-S. Zheng and Q.-F. Dong, *Phys. Chem. Chem. Phys.*, 2012, **14**, 5376–5382.
36 B. Ding, C. Yuan, L. Shen, G. Xu, P. Nie and X. Zhang, *Chem.–Eur. J.*, 2013, **19**, 1013–1019.
37 C. Liang, N. J. Dudney and J. Y. Howe, *Chem. Mater.*, 2009, **21**, 4724–4730.
38 C. Tang, B. Q. Li, Q. Zhang, L. Zhu, H. F. Wang, J. L. Shi and F. Wei, *Adv. Funct. Mater.*, 2016, **26**, 577–585.
39 Y. J. Zhong, S. F. Wang, Y. J. Sha, M. L. Liu, R. Cai, L. Li and Z. P. Shao, *J. Mater. Chem. A*, 2016, **4**, 9526–9535.
40 K. Balakumar and N. Kalaiselvi, *RSC Adv.*, 2015, **5**, 34008–34018.
41 G. Li, J. Sun, W. Hou, S. Jiang, Y. Huang and J. Geng, *Nat. Commun.*, 2016, **7**, 10601.
42 H. Wang, C. Zhang, Z. Chen, H. K. Liu and Z. Guo, *Carbon*, 2015, **81**, 782–787.
43 F. Jin, S. Xiao, L. Lu and Y. Wang, *Nano Lett.*, 2016, **16**, 440–447.
44 G. He, X. Ji and L. Nazar, *Energy Environ. Sci.*, 2011, **4**, 2878–2883.
45 B. Zhang, C. Lai, Z. Zhou and X. Gao, *Electrochim. Acta*, 2009, **54**, 3708–3713.
46 S. Kim, Y. Jung and S.-J. Park, *J. Power Sources*, 2005, **152**, 272–277.
47 S. Dörfler, M. Hagen, H. Althues, J. Tübke, S. Kaskel and M. J. Hoffmann, *Chem. Commun.*, 2012, **48**, 4097–4099.
48 J. Schuster, G. He, B. Mandlmeier, T. Yim, K. T. Lee, T. Bein and L. F. Nazar, *Angew. Chem., Int. Ed.*, 2012, **51**, 3591–3595.

49 Z. W. Seh, W. Li, J. J. Cha, G. Zheng, Y. Yang, M. T. McDowell, P.-C. Hsu and Y. Cui, *Nat. Commun.*, 2013, **4**, 1331.

50 N. Brun, K. Sakaushi, L. Yu, L. Giebeler, J. Eckert and M. M. Titirici, *Phys. Chem. Chem. Phys.*, 2013, **15**, 6080–6087.

51 L. Ji, M. Rao, H. Zheng, L. Zhang, Y. Li, W. Duan, J. Guo, E. J. Cairns and Y. Zhang, *J. Am. Chem. Soc.*, 2011, **133**, 18522–18525.

52 Y. Cao, X. Li, I. A. Aksay, J. Lemmon, Z. Nie, Z. Yang and J. Liu, *Phys. Chem. Chem. Phys.*, 2011, **13**, 7660–7665.